

1 **Effect of pipeline surface roughness on peak impact forces**
2 **caused by hydrodynamic submarine mudflow**

3 **Xingsen Guo ^{1,2,3a}, Thorsten Stoesser ^{3b,*}, Tingkai Nian ^{2c,**}, Yonggang Jia ^{1d}, Xiaolei Liu ^{1e}**

4 1. *Shandong Provincial Key Laboratory of Marine Environment and Geological Engineering,*
5 *Ocean University of China, Qingdao 266100, China*

6 2. *State Key Laboratory of Coastal and Offshore Engineering, Dalian University of Technology,*
7 *Dalian 116024, China*

8 3. *Department of Civil, Environmental, Geomatic Engineering, University College London,*
9 *London WC1E 6BT, United Kingdom*

10 * Corresponding author, Professor, Email: t.stoesser@ucl.ac.uk

11 ** Co-corresponding author, Professor, Email: tknian@dlut.edu.cn

12 ^a Ph.D., Postdoctoral Fellow of *University College London*, Email: xingsenguo@yeah.net

13 ^b Ph.D., Professor of *University College London*, Email: t.stoesser@ucl.ac.uk

14 ^c Ph.D., Professor of *Dalian University of Technology*, Email: tknian@dlut.edu.cn

15 ^d Ph.D., Professor of *Ocean University of China*, Email: yonggang@ouc.edu.cn

16 ^e Ph.D., Professor of *Ocean University of China*, Email: xiaolei@ouc.edu.cn

Abstract

17
18 The effect of pipeline surface roughness on the interaction between submarine landslides and
19 pipelines may not be insignificant and has rarely been quantified. In this paper, a previously
20 validated computational fluid dynamics model is employed to study the interaction of submarine
21 landslides and suspended or laid-on-seabed pipelines, respectively, which are roughened in order
22 to quantify the effect of pipeline surface roughness. Here, four orders of magnitude surface
23 roughnesses are chosen whereas the mudflows (submarine landslides) occur at typical Reynolds
24 numbers. The effect of surface roughness is primarily reflected in the peak load of the impact
25 forces on the pipelines, which are more sensitive to high Reynolds numbers and suspension
26 conditions. For suspended pipelines, with the increase of roughness, (i) the peak lift force
27 increases, (ii) the peak drag force decreases, and (iii) Strouhal number slightly increases.
28 Compared with nearly smooth pipelines, the relative increase of the peak lift force and the relative
29 reduction of the peak drag force on suspended pipelines with a surface roughness of 0.15 mm
30 attain 62% or 17%, respectively. Additionally, relevant mechanisms are highlighted via contours
31 of the pressure around the pipeline, the interfacial shear rate, as well as the squeeze and hindrance
32 effect of the seabed. Further, a standard chart methodology considering pipeline roughness to
33 estimate peak impact forces is established, which provides a basis for the risk assessment of the
34 whole life cycle of submarine pipelines.

Keywords

35
36 Submarine pipeline; Mudflow; Surface roughness; Peak impact forces; Influence law; Evaluation
37 methodology.

38 **1. Introduction**

39 Submarine pipelines are an indispensable asset for connecting oil and gas production fields to the
40 shore and transporting petroleum fluids from the sea to storage terminals on shore, which is
41 known as the lifeline ([Hance, 2003](#); [Gao, 2017](#)). With the development of offshore oil and gas
42 fields into deep waters, high seas and polar regions, these pipelines face a harsh marine
43 environment and are subjected to significant external loads, including waves, currents, high
44 pressure, low temperature, high salinity leading to corrosion, colonization by microorganisms
45 causing biofouling and/or even geological disasters such as submarine landslides. Hence, higher
46 quality requirements for submarine pipelines are put forward. The construction and operation
47 management of the lifeline is characterized by major investment, high risk and long return period
48 which entails that pipelines have been developed in the direction of longer distance transportation,
49 larger diameter, more service life and greater reliability in order to make oil and gas exploration
50 projects profitable quickly, which proposes greater challenges to the pipeline design.

51 As a highly-destructive but very sporadic load, submarine landslides, including debris flows
52 and mudflows, have caused great damage to submarine pipelines ([Hsu et al., 2008](#); [Dong et al.,](#)
53 [2017a](#)); hence, submarine landslide-pipeline-interaction has become a research focus ([Dong et al.,](#)
54 [2017b](#); [Nian et al., 2018](#); [Malgesini et al., 2018](#); [Qian et al., 2019](#); [Dutta and Hawlader, 2019](#);
55 [Chatzidakis et al., 2018](#); [Chen et al., 2020](#)) recently. In terms of physical tests, single-phase
56 (anhydrous environment) particle flow experiments ([Chehata et al., 2003](#); [Wang et al., 2008](#);
57 [Perez-Gruszkiewicz, 2012](#)), flume experiment ([Zakeri et al., 2008](#); [Haza et al., 2013](#)), rotating
58 flume experiment ([Wang et al., 2018](#)) and centrifugal experiments ([Zakeri et al., 2012](#)) have been
59 carried out, the related characteristics of pipeline stress were explored, and reliable methods for

60 assessing impact forces under simple working conditions were established. However, due to the
61 shortcomings of physical tests, including substantial human resources and material input, limited
62 conditions and insufficient acquisition parameters, numerical simulations have become an
63 alternative approach to investigate complex pipeline-mudflow interactions. From numerical
64 simulations, many important aspects have been revealed, including physical and mechanical
65 properties and composition of landslides (Zakeri, 2009; Nian et al., 2018), in-place state of
66 pipelines (i.e., buried (Zhu and Randolph, 2011; Dong et al., 2017b; Zhang et al., 2019a),
67 laid-on-seabed (Fan et al., 2018; Guo et al., 2019a), suspension (Zakeri et al., 2009; Qian et al.,
68 2020) and different span heights (Guo et al., 2019a)), impact angle between landslides and
69 pipelines (Zakeri, 2009; Liu et al., 2015; Zhang et al., 2019b), pipeline types (i.e., streamlined
70 (Fan et al., 2018), honeycomb-hole (Guo et al., 2019b and 2021a)) and seafloor low-temperature
71 environment (Nian et al., 2018). However, past studies have not taken into account the changes in
72 the pipeline surface condition on the landslide impact forces on the submarine pipeline during the
73 pipeline long-term service.

74 Depending on the technical requirements, the outside surface of submarine pipelines may be
75 made of concrete, steel, rubber, asphalt, polyethylene, etc. In the long-term service process, the
76 harsh marine environment accelerates the aging of the pipeline and thereby increasing their
77 surface roughness, and the accumulation of damage, and hence a reduction of bearing capacity.
78 Practically, the attachment of microorganisms further increases the pipeline surface roughness
79 (Ghazali et al., 2019). Surface roughness of structures has a significant effect on the flow field
80 around them (Zhou et al., 2015; Zeinoddini et al., 2016; Tian et al., 2019; Gao et al., 2020; Bi et
81 al., 2020), hence alters the hydrodynamic force distribution and magnitude on pipelines due to

82 landslides, which has a great influence on pipeline design. Therefore, this paper focuses on the
83 effect of pipeline surface roughness on the impact forces (i.e., drag and lift forces) on suspended
84 and laid-on-seabed pipelines caused by mudflows in a marine environment.

85 The remainder of this paper is organized as follows. In Section 2, the effect of surface
86 roughness of suspended and laid-on-seabed pipelines on submarine landslide-pipeline interaction
87 are numerically modeled and studied by the previously verified computational fluid dynamics
88 (CFD) method using an equivalent sand grain roughness model. In Section 3, the relevant
89 hydrodynamic mechanisms creating peak impact forces caused by pipeline surface roughness are
90 elucidated and discussed, and the variation of Strouhal number for assessing flow-induced
91 vibrations on the suspended pipeline is given. In Section 4, a simplified evaluation methodology to
92 estimate peak drag and lift forces is established to provide a basis for pipeline design and risk
93 assessment. The conclusions of this study are presented in Section 5.

94 **2. Methodology**

95 **2.1 CFD approach**

96 There are many numerical modelling studies simulating submarine landslide-pipeline-interaction,
97 including the computational fluid dynamics (CFD) (Zakeri, 2009; Zakeri et al., 2009; Liu et al.,
98 2015; Nian et al., 2018; Qian et al., 2019; Dutta and Hawlader, 2019; Guo et al., 2019a, 2019b and
99 2021a; Zhang et al., 2019b), large deformation finite element (LDFE) method (Zhu and Randolph,
100 2011), material point method (MPM) (Dong et al., 2017b), coupled Eulerian-Lagrangian (CEL)
101 method (Saha et al., 2018) or the particle finite element method (Zhang et al., 2019b), respectively.
102 Based on CFD, Zakeri et al. (2009) effectively reproduced the flume experiment of Zakeri et al.
103 (2008) and obtained accurate quantitative parameters. At present, CFD numerical modelling is one

104 of the most widely used methods.

105 Using CFD approach, submarine landslide-pipeline-interaction is considered to be a typical
 106 two-phase fluid-structure interactions (FSI) problem (Guo et al., 2021b). Hence, CFD
 107 incompressible two-phase flow based on the Eulerian-Eulerian multiphase flow model is adopted
 108 to model the free surface flow of continuous fluids (i.e., ambient water and submarine landslide).
 109 The ambient water (Eulerian material) and submarine landslide (Eulerian material) are denoted by
 110 α and β , respectively, and the total phase number is $N_p = 2$. Governing equations (i.e.,
 111 continuity and momentum equations) are as following:

112 Continuity equation:

$$113 \quad \frac{\partial}{\partial t}(r_\alpha \rho_\alpha) + \nabla \cdot (r_\alpha \rho_\alpha U_\alpha) = M_{MS\alpha} + \sum_{\beta=1}^{N_p} \Gamma_{\alpha\beta} \quad (1)$$

114 where r_α , ρ_α and U_α are the volume fraction, density, and velocity, respectively, of phase α ;
 115 $M_{MS\alpha}$ is the user-specified quality source phase; and $\Gamma_{\alpha\beta}$ is the mass flow rate of a unit volume
 116 from phase β to phase α , which must satisfy $\Gamma_{\alpha\beta} = -\Gamma_{\beta\alpha} \Rightarrow \sum_{\beta=1}^{N_p} \Gamma_{\alpha\beta} = 0$. For determining the
 117 direction of the mass exchange process, if $\Gamma_{\alpha\beta} = \Gamma_{\alpha\beta}^+ - \Gamma_{\beta\alpha}^+ > 0$, the mass flow rate of the unit
 118 volume from phase β to phase α is positive and the volume fraction is $\sum_{\alpha=1}^{N_p} r_\alpha = 1$.

119 Momentum equation:

$$120 \quad \frac{\partial}{\partial t}(r_\alpha \rho_\alpha U_\alpha) + \nabla \cdot (r_\alpha (\rho_\alpha U_\alpha \otimes U_\alpha)) = -r_\alpha \nabla P_\alpha + \nabla \cdot (r_\alpha \mu_\alpha (\nabla U_\alpha + (\nabla U_\alpha)^T)) + \sum_{\beta=1}^{N_p} (\Gamma_{\alpha\beta}^+ U_\beta - \Gamma_{\beta\alpha}^+ U_\alpha) + S_{M\alpha} + M_\alpha \quad (2)$$

121 where P_α and μ_α are the pressure and viscosity of phase α , respectively; $S_{M\alpha}$ is the
 122 momentum source that is caused by an external force; and M_α is the total interface force on
 123 phase α due to phase β , which can be calculated via the following equation:

$$124 \quad M_\alpha = \sum_{\beta \neq \alpha} M_{\alpha\beta} = -\sum_{\alpha \neq \beta} M_{\beta\alpha} = M_{\alpha\beta}^D + M_{\alpha\beta}^L + M_{\alpha\beta}^{LUB} + M_{\alpha\beta}^{VM} + M_{\alpha\beta}^{TD} \quad (3)$$

125 where $M_{\alpha\beta}^D$ is the interphase drag force on phase α caused by phase β ; $M_{\alpha\beta}^L$ is the lift force

126 on phase α caused by phase β ; $M_{\alpha\beta}^{LUB}$ is the wall lubrication force on phase α caused by
127 phase β ; $M_{\alpha\beta}^{VM}$ is the virtual mass force on phase α caused by phase β ; $M_{\alpha\beta}^{TD}$ is the
128 turbulence dispersion force on phase α caused by phase β . The non-drag forces are mainly used
129 for discrete phases. This study only considers the drag force between phases.

130 **2.2 Rheological model of submarine mudflows**

131 Submarine landslides have a clear stage division in their evolutionary process (Locat and Lee,
132 2002; Hance, 2003; Shanmugam, 2015). Earthquakes (Rodríguez-Ochoa et al., 2015; Rashid et al.,
133 2017; Nian et al., 2019; Guo et al., 2020a), hydrate decomposition (Hance, 2003; He et al., 2013;
134 Elger et al., 2018; Chen et al., 2020) and other causes triggered the instability of submarine slopes.
135 The landslide detaches from the submarine slope is inevitably undergoing evolution from a block
136 slip, a mud/debris flow, a turbidity flow, to a heavy water flow and finally sedimentation.
137 Currently, CFD modelling is employed to simulate and analyze submarine landslides impacting on
138 pipelines. Hence, detailed assessment is needed to determine which stage of the landslide to adopt
139 in CFD. Two factors are primarily considered: (i) probability of occurrence; (ii) destructive power.
140 For submarine landslides at the stage of a mud/debris flow, their migration range is wider than for
141 the block slip stage, which leads to a higher probability of pipeline impact; their density and shear
142 strength are larger than for the turbidity flow and heavy water flow stages, and their flow velocity
143 is higher than for the other stages, which leads to more destructive force (Bruschi et al., 2006) in
144 comparison to the other stages; thus, most researchers consider the stage of mud/debris flow for
145 analysis of landslide-pipeline-interaction.

146 Submarine mud/debris flows have non-Newtonian fluid properties and are often described
147 using a non-Newtonian fluid with shear thinning characteristics. The submarine mudflows adopted

148 in this paper come from the northern deep-water continental slope of the South China Sea.
149 Through in-situ sampling, low-temperature rheological parameters of submarine mudflows are
150 tested in the laboratory. Based on the Herschel-Bulkley model shown in Eq. (4), the coupled
151 temperature-water content rheological model of mudflows has been established (Guo et al.,
152 2020b), and the rheological model is further implemented in the CFD model. Specific parameters
153 of the rheological model are reported in Table 1.

$$154 \quad \tau = \tau_y + K\dot{\gamma}^n \quad (4)$$

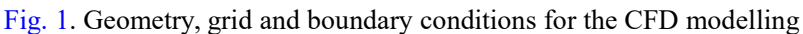
155 where τ_y is the yield stress of the submarine mudflow (Pa); K is the consistency factor of the
156 submarine mudflow ($\text{Pa}\cdot\text{s}^n$); and n is the fluidity index of the submarine mudflow.

157 **Table 1.** Herschel-Bulkley rheological model of submarine mudflows at 0.5 °C low-temperature
158 and mudflow impacting on pipeline conditions (modified after Guo et al. (2020b))

159 **2.3 CFD model and setting of boundary conditions**

160 The CFD model ANSYS CFX is employed here and it is parallelized via the platform of MPI. The
161 CFD model is based on the method of finite volumes. The computational domain and the impact
162 velocity of the landslide are determined by a methodology from the previous study (Guo et al.,
163 2018), ensuring that the simulation results effectively correspond to engineering practice. In
164 practical projects, submarine pipelines are mostly laid on the seabed surface, especially deep-sea
165 pipelines. In the long-term service process, the submarine pipeline will inevitably have a
166 suspended span, including marine soils below pipelines eroded by active bottom currents (Zhao et
167 al., 2021), and submarine pipelines cross areas with high topographic relief (Guo et al., 2019a).
168 Therefore, the two most common types of pipelines in deep-sea areas (i.e., laid-on-seabed and
169 suspended pipelines) are considered. Through the engineering monitoring, most submarine

170 pipelines have a span height of approximately one times the diameter of the pipeline (Huang et al.,
171 2021), and thus the span height of the suspended pipeline is set to 1 times the pipeline diameter.
172 The geometry, grid and boundary conditions for CFD modelling are presented in Fig. 1. Using
173 grids with a grid quality (i.e., an important and comprehensive parameter to evaluate the grid
174 division in ANSYS ICEM CFD, where 0 is poor and 1 is good) of greater than 0.8, grid sensitivity
175 analyses are carried out to ensure the reliability and credibility of the results. Based on a
176 two-phase free surface flow model, the submarine mudflow is described by Eulerian continuous
177 fluid material, and no turbulence model is employed due to its highly-viscous and non-Newtonian
178 nature (Guo et al., 2021c). The ambient water is also described by Eulerian continuous fluid
179 material, and turbulence is accounted for using the $k-\varepsilon$ turbulence model. The simulation is
180 transient with a total time of 1 s and a time step of 0.001 s; more details are provided in Nian et al.
181 (2008) and Guo et al. (2019a, 2019b and 2021a).

182  Fig. 1. Geometry, grid and boundary conditions for the CFD modelling

183 **2.4 Equivalent sand grain roughness model**

184 The main objective here is to study the effect of surface roughness which refers to the effective
185 unevenness of the pipeline's outer surface with small peaks and troughs, the smaller the surface
186 roughness, the smoother the object. The surface friction of a submarine pipeline depends not only
187 on the roughness height but also on the roughness type (i.e., shape, distribution, density, etc.)
188 (Coleman et al., 1984; White, 1991; Adams et al., 2012). In this paper, it is assumed that the
189 distribution of surface roughness on submarine pipelines is uniform, and based on the equivalent
190 sand grain roughness model (Adams et al., 2012). Figure 2 presents specific settings of the
191 pipeline surface roughness. A layer of closely packed spheres on a submarine pipeline provides an

192 average roughness height. Surface roughness model alters the fluid velocity near the wall (i.e.,
193 pipeline surface), resulting in changes in the shear stress near the pipeline, affecting the flow field
194 around the pipeline, and causing changes in the forces on the pipeline (Coleman et al., 1984;
195 White, 1991). By setting the equivalent sand grain roughness k_s to four different orders of
196 magnitude (i.e., 0 mm, 0.0015 mm, 0.015 mm and 0.15 mm), in which a large number of past
197 studies use a roughness of 0.0015 mm, the no slip wall boundary condition (i.e., the no slip wall
198 boundary condition means that there is no relative sliding between the fluid and boundary wall,
199 that is, the tangential velocity at the wall surface is zero) allows quantification of the effect of
200 surface roughness. The pipeline surface roughness settings are given in Table 2, and the
201 corresponding simulations are detailed in Tables 1 and 2.

202 Fig. 2. Equivalent sand grain roughness model; (a) applied to seabed; (b) applied to submarine
203 pipeline

204 Table 2. Specific settings of pipeline surface roughness

205 2.5 Verification of CFD approach

206 Based on the CFD approach described above, the numerical modelling of a submarine landslide
207 impact on a pipeline under the action of the ambient water can be established to evaluate the
208 impact forces on the submarine pipeline. Compared with the past flume tests (Zakeri et al., 2008
209 and 2009) and the CFD numerical simulation method (Zakeri, 2009; Liu et al., 2015), this CFD
210 approach used by the authors in this paper has been validated several times (Nian et al., 2018; Guo
211 et al., 2019a, 2019b and 2021a). Specifically, the rheological model of a submarine landslide from
212 Si (2007) used by Zakeri (2009) and Liu et al. (2015) is used to simulate the submarine landslide,
213 the span height of the submarine pipeline is set as 2.5 times the pipeline diameter, the surface

214 roughness of the pipeline is taken as 0.0015 mm, and other settings of the computational domain
215 are consistent with Section 2.3. Compared with the numerical results of previous CFD simulations
216 from Zakeri (2009) and Liu et al. (2015), the simulation results of the CFD modelling used by the
217 authors in this paper fall somewhere in between, and the differences are small, which verifies the
218 accuracy of the CFD numerical model, as shown in Table 3.

219 Table 3. Simulation results of the drag force coefficient under three Reynolds number conditions
220 in different studies

221 3. Results and discussions

222 3.1 Results

223 First of all, impact forces (i.e., the horizontal drag force and vertical lift force) acting on the
224 submarine pipeline are extracted from the numerical results. The Reynolds number of the flow is
225 346.47, a typical representative flow, and time-force curves for submarine mudflow impact on
226 pipelines with different surface roughness conditions are presented in Figs. 3 and 4, showing
227 suspended pipeline and laid-on-seabed pipeline, respectively. Evidently, surface roughness
228 primarily affects the peak of the impact forces, but has a small effect on the base load on the
229 pipeline. Among them, under the suspension condition, the reduction rate of a peak drag force on a
230 pipeline with the surface roughness of 0.15 mm reaches 17% compared with a nearly smooth
231 pipeline, and the increase rate of a peak lift force even reaches 62%. The lift force is more affected
232 than the drag force.

233 Fig. 3. Impact forces as a function of time for suspended pipelines with different surface
234 roughness at Reynolds number 346.47

235 [Fig. 4](#). Impact forces as a function of time for laid-on-seabed pipelines with different surface
236 roughness at Reynolds number 346.47

237 Peak loads for a wider range of working conditions (in terms of Reynolds number) are
238 acquired. [Figure 5](#) presents peak impact forces as a function of Reynolds number for different
239 surface roughnesses. For the suspended pipeline, with the increase in pipeline surface roughness,
240 the peak drag force gradually decreases, and the peak lift force gradually increases; under the
241 condition of low Reynolds number (< 10), the influence of pipeline surface roughness is
242 insignificant; with the increase in Reynolds number, the effect of surface roughness is becoming
243 more and more prominent. For the laid-on-seabed pipeline, the effect of pipeline surface
244 roughness on peak impact forces at different Reynolds numbers is very complex due to the
245 interaction of the flow with the seabed. In general, the effect of roughness on the laid-on-seabed
246 pipeline is basically the same as that of the suspended pipeline, and it is more significant at high
247 Reynolds numbers. Additionally, the pipeline surface roughness is more sensitive and has been a
248 more significant influence on the suspended pipeline.

249 [Fig. 5](#). Peak impact forces as a function of Reynolds number for different surface roughnesses

250 **3.2 Effect of pipeline roughness on flow mechanisms**

251 The drag force can be divided into pressure drag and friction drag. A thin boundary layer is formed
252 on the pipeline surface because of the mudflow's viscosity. The greater the shear rate (i.e., velocity
253 gradient) of the mudflow in the boundary layer, the greater the frictional drag; pipeline surface
254 roughness affects the shear rate; thus, frictional drag is closely related to the pipeline's surface
255 roughness. [Figure 6](#) presents contours of (a) pressure and (b) shear rate for suspended pipelines
256 with smooth and rough ($k_s = 0.15$ mm) surfaces at selected instants in time and Reynolds number

257 346.47. Specifically, the influence of the pipeline surface roughness on mudflows impacting on
258 pipelines is a typical interface contact problem. At different moments when the mudflow passes
259 the pipeline with different surface roughnesses, different shear rates are generated. The greater the
260 pipeline surface roughness, the greater the shear rate on the pipeline surface, and the higher the
261 shear stress. Noticeably, the friction drag depends on the resultant shear stresses along the impact
262 force direction. In parallel, the impact forces on the pipeline are also analyzed by the pressure
263 difference between the two sides of the pipeline along the direction of flow. In other words, the
264 greater the pressure difference, the greater the drag force in the horizontal direction and the greater
265 the lift force in the vertical direction. The root cause of the pressure variation is the change in the
266 velocity field of the mudflow around the pipeline. An increase in pipeline surface roughness
267 reduces the acceleration of the mudflow around the pipeline to a certain extent, which plays a role
268 in reducing the drag force and enhancing the lift force, and is similar to the principle of flow
269 around a golf-ball (Guo et al., 2019b and 2021a). Therefore, the combined shear stress and
270 differential pressures causes very complex pipeline forces, as presented in Fig. 5.

271 Fig. 6. Contours of (a) pressure and (b) shear rate for suspended pipelines with smooth and rough
272 ($k_s = 0.15$ mm) surfaces at selected instants in time and at Reynolds number 346.47

273 For suspended pipelines, when the mudflow approaches the pipeline, the pressure difference
274 on the pipeline is larger because the area of negative pressure behind the pipeline is larger, which
275 causes the peak impact forces, as plotted in Fig. 6. When the mudflow has passed the pipeline and
276 forms a backflow, the absolute value of the negative pressure is significantly reduced, and a
277 relatively small pressure difference is formed, which is considered stable impact force.

278 The biggest difference in the force mechanism between a laid-on-seabed pipeline and a

279 suspended pipeline is the influence of the seabed. [Figure 7](#) presents contours of (a) pressure and (b)
280 shear rate for the laid-on-seabed pipelines with smooth and rough ($k_s = 0.15$ mm) surfaces at
281 selected instants in time and at Reynolds number 346.47. Due to the seabed, the positive pressure
282 zone on the upstream side of the pipeline is shifted downwards, while the negative pressure zone
283 on the downstream side is shifted upwards. At the same time, the part where the pipeline is in
284 contact with the seabed hinders the mudflow, and the minimal gap between the pipeline and the
285 seabed has a squeeze effect on the mudflow that flows through the gap. Both effects result in a
286 larger pressure difference, a higher shear rate, and a more unbalanced distribution for the
287 laid-on-seabed pipeline in comparison to the suspended pipeline. Under different impact velocities
288 (i.e., Reynolds number), the influence characteristic of impact forces is more complicated.

289 [Fig. 7](#). Contours of the (a) pressure and (b) shear rate for the laid-on-seabed pipelines with smooth
290 and rough ($k_s = 0.15$ mm) at selected instants in time and at Reynolds number 346.47

291 **3.3 Vibration characteristics of lift force on suspended pipeline**

292 Another factor that cannot be ignored for suspended pipelines is the flow-induced vibration of the
293 pipeline due to the oscillating the lift force. However, according to the simulation results, the
294 laid-on-seabed pipeline does not cause vibration of the lift force. A lifeline project pays great
295 attention to the vibration frequency in order to prevent resonance of the submarine pipeline
296 structure. The Strouhal number is an important characteristic parameter for analyzing the
297 fluid-structure interaction and the flow-induced vibration, and its definition is given in [Eq. \(5\)](#).

$$298 \quad St = \frac{f \cdot D}{U_\infty} \quad (5)$$

299 where St is the Strouhal number, which is a dimensionless parameter; and f is the frequency of

300 vortex shedding (Hz).

301 The vibration frequency of the lift force can be estimated if the Strouhal number is known.
302 Studies have shown that the Strouhal number is related to the Reynolds number, and in a certain
303 range of Reynolds numbers ($Re > 300$), the Strouhal number attains a constant value (Roshko,
304 1961). Based on the simulation results (Nian et al., 2018; Guo et al., 2019a and 2019b), the strong
305 fluctuation of the lift force on the suspended pipeline occurs when the Reynolds number is greater
306 than 50. Figure 8 presents contours of the velocity distribution for the suspended pipeline at
307 Reynolds number 346.47, demonstrating the generation process of vortexes behind the pipeline
308 that causes flow-induced vibration. The Strouhal number tends to increase with increasing
309 pipeline surface roughness. Figure 9 plots the Strouhal number as a function of Reynolds number
310 for the simulated cases and the flume experiments of Zakeri et al. (2008). The numerical
311 simulations cover a wider range of Reynolds numbers. The values of St range from 0.16 to 0.18.

312 Fig. 8. Contours of velocity distribution for the suspended pipeline at Reynolds number 346.47; (a)
313 smooth pipeline; (b) pipeline with $k_s = 0.15$ mm

314 Fig. 9. Strouhal number as a function of Reynolds number

315 4. Calculation methodology to predict peak impact forces

316 In order to predict impact forces at different working conditions, a method for calculating the drag
317 force coefficient and lift force coefficient is proposed. Based on the analysis in the previous
318 sections, using peaks of the impact forces as the characteristic values, the equations for calculating
319 the peak drag and lift force coefficients are given as,

$$320 C_{D-P} = \frac{2F_{D-P}}{\rho \cdot U_{\infty}^2 \cdot A_{fm}} \quad (6)$$

321
$$C_{L-P} = \frac{2F_{L-P}}{\rho \cdot U_{\infty}^2 \cdot A_{/m}} \quad (7)$$

322 where C_{D-P} and C_{L-P} are the peak drag force coefficient and peak lift force coefficient, respectively,
 323 which are dimensionless parameters; F_{D-P} and F_{L-P} are the peak drag force and peak lift force
 324 caused by the submarine mudflow on the pipeline per m, respectively (N); and $A_{/m}$ is the projected
 325 areas of the submarine pipeline per m along impact direction (m^2). The projected areas of the
 326 submarine pipeline per m along impact force direction are calculated as follows.

327
$$A_{/m} = (D + k_s) \times 1m \quad (8)$$

328 where $A_{/m}$ is the projected areas of the submarine pipeline per m along impact force direction.

329 Based on Eqs. (6), (7) and (8), the peak impact forces as quantified in Fig. 5 are converted
 330 into peak impact forces coefficients, as presented in Fig. 10. Since the two independent variables,
 331 the peak drag force coefficient and peak lift force coefficient, are related to the three dependent
 332 variables of the pipeline, i.e., placement, surface roughness and Reynolds number, the variation of
 333 the coefficient is very complex and difficult to describe by simple formulae. Hence, a chart
 334 (commonly used in engineering) is established to obtain the peak impact force coefficients under
 335 multi-parameter conditions. First, the surface roughness adjustment factor \mathcal{K} is proposed, and
 336 the factor \mathcal{K} is related to RDR , span height and Reynolds number, as presented in Eq. (9). The
 337 effects of these three factors on \mathcal{K} are coupled together, and thus equation (9) is a very complex
 338 function and difficult to quantify by simply multiplying these three parameters. Second, the peak
 339 drag force coefficient and peak lift force coefficient of nearly smooth pipelines are used as the
 340 standard value. Third, the product of \mathcal{K} and the standard value represents the peak impact force
 341 coefficients under the current working condition, as shown in Eqs. (11) and (12).

342
$$\kappa = f(RDR, \text{Span height}, \text{Re}_{\text{non-Newtonian}})$$
 (9)

343 where κ is the surface roughness adjustment factor for considering the force evaluation of
 344 submarine mudflows impact pipelines, which is a dimensionless parameter; and RDR is the ratio
 345 of the surface roughness to the submarine pipeline diameter, which a dimensionless parameter, and
 346 the equation is given in Eq. (10).

347
$$RDR = \frac{k_s}{D}$$
 (10)

348 where k_s is the surface roughness of the submarine pipeline (mm).

349
$$C_{D-P}^{\text{other roughness}} = \kappa \cdot C_{D-P}^{\text{smooth}}$$
 (11)

350
$$C_{L-P}^{\text{other roughness}} = \kappa \cdot C_{L-P}^{\text{smooth}}$$
 (12)

351 where, $C_{D-P}^{\text{other roughness}}$ and $C_{L-P}^{\text{other roughness}}$ are the peak drag force coefficient and peak lift force
 352 coefficient to be solved, respectively, which are dimensionless parameters; and C_{D-P}^{smooth} and
 353 C_{L-P}^{smooth} are the standard values of peak drag force coefficient and peak lift force coefficient,
 354 respectively, which are dimensionless parameters.

355 **Fig. 10.** Peak impact force coefficients as a function of Reynolds number for different surface
 356 roughnesses

357 In reference to Fig. 10, the peak impact force coefficients are divided by the standard value to
 358 obtain the surface roughness adjustment factor under different RDR conditions. Based on a cubic
 359 spline interpolation function, the piecewise smooth curves are drawn, and the charts, as presented
 360 in Fig. 11, are obtained. RDR values not plotted in these charts can be obtained by interpolation
 361 between adjacent curves. In addition, if there is no standard value (nearly smooth condition), it is
 362 converted into a standard value by the κ conversion. The methodology is very simple, efficient
 363 and convenient for pipeline designers, and intuitively includes the effect of pipeline surface

364 roughness on peak impact forces during the life cycle of submarine pipelines. In summary,
365 submarine pipelines with different materials need to be carefully checked for surface roughness
366 and potentially modify the peak impact forces before design and construction.

367 [Fig. 11](#). Standard evaluation charts for the surface roughness adjustment factor

368 **5. Conclusions**

369 A CFD approach is employed to investigate and quantify the effect of pipeline surface roughness
370 on hydrodynamic loads due to submarine mudflows for suspended and laid-on-seabed pipelines.

371 The main conclusions that can be drawn are:

372 (1) Pipeline surface roughness primarily affects the peak load of impact forces on submarine
373 pipelines; however, it has little influence on their stable load. Compared with nearly smooth
374 pipelines, the reduction of peak drag force of submarine pipelines with a $k_s = 0.15$ mm rough
375 surface roughness reaches 17%, and the increase of peak lift force even reaches 62% in
376 comparison to the smooth surface counterpart.

377 (2) Considering various conditions of the pipeline, including placement, surface roughness and
378 Reynolds number, the effect of roughness on peak impact forces is very complex. Generally
379 speaking, with an increase in roughness, the peak drag force decreases, while the peak lift force
380 increases; the roughness is much more sensitive for high Reynolds number flows and varies with
381 suspension condition.

382 (3) As a typical interface contact problem, the influence mechanism of different pipeline surface
383 roughnesses under multiple complex conditions is systematically analyzed using shear stress,
384 pressure difference, evolution of interface shear rate, and squeeze and hindrance effect of the
385 seabed. It has been found that the greater the pipeline surface roughness, the greater the shear rate,

386 the higher the shear stress, and the lower the acceleration of the mudflow and the relatively
387 smaller the pressure difference around the pipeline; due to the seabed, the positive pressure zone
388 on the upstream side of the pipeline is shifted downwards, while the negative pressure zone on the
389 downstream side is shifted upwards.

390 (4) The Strouhal number is used to estimate the vibration frequency of the lift force in order to
391 prevent resonance of submarine pipelines. The Strouhal number (St) slightly increases with
392 increasing pipeline surface roughness; it is established that St is between 0.16 and 0.18.

393 (5) A surface roughness adjustment factor for rough submarine pipeline is proposed, and charts of
394 their distribution as a function of Re are provided for the two placement conditions investigated
395 here. An evaluation methodology based on these charts to adjust the peak drag force coefficient
396 and peak lift force coefficient due to pipeline roughness is established, which provides a basis for
397 the design of submarine pipelines over their life cycle.

398 **Acknowledgments**

399 Funding for the research has been supported by the National Key Research and Development
400 Program of China (No. 2018YFC0309203), the National Natural Science Foundation of China
401 (No. 51879036), the LiaoNing Revitalization Talents Program (No. XLYC2002036), and the
402 China Scholarship Council (CSC) during a visit of Xingsen Guo to the Department of Civil,
403 Environmental, Geomatic Engineering (CEGE) of University College London (UCL). This
404 support is gratefully acknowledged.

405 **Availability of data and materials**

406 All data, models, and code generated or used during the study appear in the submitted article.

407 **References**

- 408 Adams, T., Grant, C., Watson, H., 2012. A simple algorithm to relate measured surface roughness
409 to equivalent sand-grain roughness. *International Journal of Mechanical Engineering and*
410 *Mechatronics*, 1 (2), 66–71. <https://doi.org/10.11159/ijmem.2012.008>
- 411 Bi, C.W., Chen, Q.P., Zhao, Y.P., Su, H., Wang, X.Y., 2020. Experimental investigation on the
412 hydrodynamic performance of plane nets fouled by hydroids in waves. *Ocean Eng.*, 213,
413 107839. <https://doi.org/10.1016/j.oceaneng.2020.107839>
- 414 Bruschi, R., Bughi, S., Spinazzè, M., Torselletti, E., Vitali, L., 2006. Impact of debris flows and
415 turbidity currents on seafloor structures. *Norwegian Journal of Geology/Norsk Geologisk*
416 *Forening*, 86 (3), 317–336.
- 417 Chatzidakis, D., Tsompanakis, Y., Psarropoulos, P.N., 2019. An improved analytical approach for
418 simulating the lateral kinematic distress of deepwater offshore pipelines. *Appl. Ocean. Res.*,
419 90, 101852. <https://doi.org/10.1016/j.apor.2019.101852>
- 420 Chehata, D., Zenit, R., Wassgren, C.R., 2003. Dense granular flow around an immersed cylinder.
421 *Phys. Fluids*, 15 (6), 1622–1631. <https://doi.org/10.1063/1.1571826>
- 422 Chen, Y.M, Zhang, L.L., Liao, C.C., Jiang, M.J., Peng, M., 2020. A two-stage probabilistic
423 approach for the risk assessment of submarine landslides induced by gas hydrate exploitation.
424 *Appl. Ocean. Res.*, 99, 102158. <https://doi.org/10.1016/j.apor.2020.102158>
- 425 Coleman, H.W., Hodge, B.K., Taylor, R.P, 1984. A re-evaluation of Schlichting’s surface
426 roughness experiment. *J. Fluids Eng.*, 106 (1), 60–65. <https://doi.org/10.1115/1.3242406>
- 427 Dong, Y., Wang, D., Randolph, M.F., 2017b. Investigation of impact forces on pipeline by
428 submarine landslide using material point method. *Ocean Eng.*, 146, 21–28.

429 <https://doi.org/10.1016/j.oceaneng.2017.09.008>

430 Dong, Y., Wang, D., Randolph, M.F., 2017a. Runout of submarine landslide simulated with
431 material point method. *Journal of Hydrodynamics*, 29 (3), 438–444.
432 [https://doi.org/10.1016/S1001-6058\(16\)60754-0](https://doi.org/10.1016/S1001-6058(16)60754-0)

433 Dutta, S., Hawlader, B., 2019. Pipeline–soil–water interaction modelling for submarine landslide
434 impact on suspended offshore pipelines. *Géotechnique*, 69 (1), 29–41.
435 <https://doi.org/10.1680/jgeot.17.P.084>

436 Elger, J., Berndt, C., Rüpke, L., Krastel, S., Gross, F., Geissler, W.H., 2018. Submarine slope
437 failures due to pipe structure formation. *Nat. Commun.*, 9 (1), 1–6.
438 <https://doi.org/10.1038/s41467-018-03176-1>

439 Fan, N., Nian, T.K., Jiao, H.B., Jia, Y.G., 2018. Interaction between submarine landslides and
440 suspended pipelines with a streamlined contour. *Mar. Georesour. Geotec.*, 36 (6), 652–662.
441 <https://doi.org/10.1080/1064119X.2017.1362084>

442 Gao, Y., Liu, L., Zou, L., Zhang, Z., Yang, B., 2020. Effect of surface roughness on
443 vortex-induced vibrations of a freely vibrating cylinder near a stationary plane wall. *Ocean*
444 *Eng.*, 198, 106837. <https://doi.org/10.1016/j.oceaneng.2019.106837>

445 Gao, F.P., 2017. Flow-pipe-soil coupling mechanisms and predictions for submarine pipeline
446 instability. *Journal of Hydrodynamics*, 29 (5), 763–773.
447 [https://doi.org/10.1016/S1001-6058\(16\)60787-4](https://doi.org/10.1016/S1001-6058(16)60787-4)

448 Ghazali, M.K.M., Shaharuddin, N.M.R., Ali, A., Siang, K.H., Nasir, M.N.M., Talib, M.H.A., 2019.
449 Surface Roughness Effect on Vortex-Induced Vibration Phenomenon in Cross-Flow Direction
450 of a Bluff Body. *Journal of Advanced Research in Fluid Mechanics and Thermal Sciences*,

451 64 (2), 253–263.

452 Guo, X.S., Nian, T.K., Wang, D., Gu, Z.D., 2021b. Evaluation of undrained shear strength of
453 surficial marine clays using ball penetration-based CFD modelling. *Acta Geotechnica*, .
454 <https://doi.org/10.1007/s11440-021-01347-x>

455 Guo, X.S., Nian, T.K., Fan, N., Jia, Y.G., 2021a. Optimization design of a honeycomb-hole
456 submarine pipeline under a hydrodynamic landslide impact. *Marine Georesources &
457 Geotechnology*, 39 (9), 1055–1070. <https://doi.org/10.1080/1064119X.2020.1801919>

458 Guo, X.S., Nian, T.K., Gu, Z.D., Li, D.Y., Fan, N., Zheng, D.F., 2021c. Evaluation Methodology
459 of Laminar-Turbulent Flow State for Fluidized Material with Special Reference to Submarine
460 Landslide. *J. Waterway, Port, Coastal, Ocean Eng.*, 147 (1), 04020048.
461 [https://doi.org/10.1061/\(ASCE\)WW.1943-5460.0000616](https://doi.org/10.1061/(ASCE)WW.1943-5460.0000616)

462 Guo, X.S., Nian, T.K., Wang, F.W., Zheng, L., 2019b. Landslides impact reduction effect by using
463 honeycomb-hole submarine pipeline. *Ocean Eng.*, 187, 106155.
464 <https://doi.org/10.1016/j.oceaneng.2019.106155>

465 Guo, X.S., Nian, T.K., Wang, Z.T., Zhao, W., Fan, N., Jiao, H.B., 2020b. Low-Temperature
466 Rheological Behavior of Submarine Mudflows. *J. Waterway, Port, Coastal, Ocean Eng.*, 146
467 (2), 04019043. [https://doi.org/10.1061/\(ASCE\)WW.1943-5460.0000551](https://doi.org/10.1061/(ASCE)WW.1943-5460.0000551)

468 Guo, X.S., Nian, T.K., Zheng, D.F., Yin, P., 2018. A methodology for designing test models of the
469 impact of submarine debris flows on pipelines based on Reynolds criterion. *Ocean Eng.*, 166,
470 226–231. <https://doi.org/10.1016/j.oceaneng.2018.08.027>

471 Guo, X.S., Zheng, D.F., Nian, T.K., Lv, L.T., 2020a. Large-scale seafloor stability evaluation of
472 the northern continental slope of South China Sea. *Mar. Georesour. Geotec.*, 38 (7), 804–817.

473 <https://doi.org/10.1080/1064119X.2019.1632996>

474 Guo, X.S., Zheng, D.F., Nian, T.K., Yin, P., 2019a. Effect of different span heights on the pipeline
475 impact forces induced by deep-sea landslides. *Appl. Ocean. Res.*, 87, 38–46.
476 <https://doi.org/10.1016/j.apor.2019.03.009>

477 Hance, J.J., 2003. Submarine Slope Stability, The University of Texas at Austin.
478 <https://www.bsee.gov/sites/bsee.gov/files/tap-technical-assessment-program/421ab.pdf>

479 Haza, Z.F., Harahap, I.S.H., 2013. Drag force investigation in the collision between subaqueous
480 mudflows and pipeline. In *2013 IEEE Business Engineering and Industrial Applications*
481 *Colloquium (BEIAC)*, 510–514. <https://doi.org/10.1109/BEIAC.2013.6560180>

482 He, Y., Zhong, G.F., Wang, L.L., Kuang, Z.G., 2013. Characteristics and occurrence of submarine
483 canyon-associated landslides in the middle of the northern continental slope, South China Sea.
484 *Mar. Petrol. Geol.*, 57 (2), 546–560. <https://doi.org/10.1016/j.marpetgeo.2014.07.003>

485 Hsu, S.K., Kuo, J., Lo, C.L., Tsai, C.H., Doo, W.B., Ku, C.Y., Sibuet, J.C., 2008. Turbidity
486 currents, submarine landslides and the 2006 Pingtung earthquake off SW Taiwan. *Terr. Atmos.*
487 *Ocean. Sci.*, 19 (6), 767–772. [https://doi.org/10.3319/TAO.2008.19.6.767\(PT\)](https://doi.org/10.3319/TAO.2008.19.6.767(PT))

488 Huang, M., Xu, J., Luan, Z., Liu, M., Li, X., Liu, B., 2021. Analysis of DF1-1 subsea pipeline
489 free-span distribution characteristics and rectification effects. *Marine Sciences*, 45 (3): 77-87.
490 (in Chinese)

491 Liu, J., Tian, J., Yi, P., 2015. Impact forces of submarine landslides on offshore pipelines. *Ocean*
492 *Eng.*, 95, 116–127. <https://doi.org/10.1016/j.oceaneng.2014.12.003>

493 Locat J., Lee H.J., 2002. Submarine landslides: advances and challenges. *Can. Geotech. J.*, 39 (1),
494 193–212. <https://doi.org/10.1139/t01-089>

495 Malgesini, G., Terrile ,E., Zuccarino, L., Parker, E., Friedmann, Y., 2018. Evaluation of Debris
496 Flow Impact on Submarine Pipelines: A Methodology, In Offshore Technology Conference.
497 Offshore Technology Conference. <https://doi.org/10.4043/28847-MS>

498 Nian, T.K., Guo, X.S., Fan, N., Jiao, H.B., Li, D.Y., 2018. Impact forces of submarine landslides
499 on suspended pipelines considering the low-temperature environment. *Appl. Ocean. Res.*, 81,
500 116–125. <https://doi.org/10.1016/j.apor.2018.09.016>

501 Nian, T.K., Guo, X.S., Zheng, D.F., Xiu, Z.X., Jiang, Z.B., 2019. Susceptibility assessment of
502 regional submarine landslides triggered by seismic actions. *Appl. Ocean. Res.*, 93, 101964.
503 <https://doi.org/10.1016/j.apor.2019.101964>

504 Perez-Gruszkiewicz, SE., 2012. Reducing underwater-slide impact forces on pipelines by
505 streamlining. *J. Waterway, Port, Coastal, Ocean Eng.*, 138 (2), 142–148.
506 [https://doi.org/10.1061/\(ASCE\)WW.1943-5460.0000113](https://doi.org/10.1061/(ASCE)WW.1943-5460.0000113)

507 Qian, X., Das, H.S., 2019. Modeling Subsea Pipeline Movement Subjected to Submarine
508 Debris-Flow Impact. *J. Pipeline Syst. Eng.*, 10 (3), 04019016.
509 [https://doi.org/10.1061/\(ASCE\)PS.1949-1204.0000386](https://doi.org/10.1061/(ASCE)PS.1949-1204.0000386)

510 Qian, X., Xu, J., Bai, Y., Das, H.S., 2020. Formation and estimation of peak impact force on
511 suspended pipelines due to submarine debris flow. *Ocean Eng.*, 195, 106695.
512 <https://doi.org/10.1016/j.oceaneng.2019.106695>

513 Rashid, H., Mackillop, K., Sherwin, J., Piper, D.J.W., Marche, B., Vermooten, M., 2017. Slope
514 instability on a shallow contourite-dominated continental margin, southeastern grand banks,
515 eastern canada. *Mar. Geol.*, 393, 203–215. <https://doi.org/10.1016/j.margeo.2017.01.001>

516 Rodríguez-Ochoa, R., Nadim, F., Hicks, M.A., 2015. Influence of weak layers on seismic stability

517 of submarine slopes. *Mar. Petrol. Geol.*, 65, 247–268.
518 <https://doi.org/10.1016/j.marpetgeo.2015.04.007>

519 Roshko, A., 1961. Experiments on the flow past a circular cylinder at very high Reynolds number.
520 *J. Fluid Mech.*, 10 (3), 345–356. <https://doi.org/10.1017/S0022112061000950>

521 Saha, D., Hawlader, B., Dutta, S., Dhar, A., 2018. A comparison using two numerical approaches
522 for modelling the impact of submarine landslides on suspended pipelines. *proceedings of*
523 *GeoEdmonton*. http://www.engr.mun.ca/~bipul/publications/saha_geoedmonton.pdf

524 Shanmugam G., 2015. The landslide problem. *Journal of Palaeogeography*, 4 (2), 109–166.
525 <https://doi.org/10.3724/SP.J.1261.2015.00071>

526 Si G., 2007. Experimental Study of the Rheology of Fine-grained Slurries and Some Numerical
527 Simulations of Downslope Slurry Movements, Masters Thesis, University of Oslo, Oslo,
528 Norway.

529 Tian, X., Li, D., Liu, G., Xie, Y., Deng, W., Xie, D., 2019. Experimental study on the
530 hydrodynamic characteristics of cylinder with rough surface. *J. Mar. Sci. Technol.*, 1–7.
531 <https://xs.scihub.ltd/https://doi.org/10.1007/s00773-019-00684-7>

532 Wang, F., Dai, Z., Nakahara, Y., Sonoyama, T., 2018. Experimental study on impact behavior of
533 submarine landslides on undersea communication cables. *Ocean Eng.*, 148, 530–537.
534 <https://doi.org/10.1016/j.oceaneng.2017.11.050>

535 Wang, L.Z., Miao, C.Z., 2008. Pressure on submarine pipelines under slowly sliding mud flows.
536 *Chinese J. Geot. Eng.*, 30 (7), 982–987. (in Chinese)
537 http://manu31.magtech.com.cn/Jwk_ytgxcb/EN/Y2008/V30/I7/982

538 White, F.M., 1991. *Viscous Fluid Flow*. 2nd edition McGraw-Hill, New York.

539 Zakeri, A., 2009. Submarine debris flow impact on suspended (free-span) pipelines: Normal and
540 longitudinal drag forces. *Ocean Eng.*, 36 (6-7), 489–499.
541 <https://doi.org/10.1016/j.oceaneng.2009.01.018>

542 Zakeri, A., Hawlader, B., Chi, K., 2012. Drag forces caused by submarine glide block or
543 out-runner block impact on suspended (free-span) pipelines. *Ocean Eng.*, 47, 50–57.
544 <https://doi.org/10.1016/j.oceaneng.2012.03.016>

545 Zakeri, A., Høeg, K., Nadim, F., 2008. Submarine debris flow impact on pipelines—Part I:
546 Experimental investigation. *Coastal Eng.*, 55 (12), 1209–1218.
547 <https://doi.org/10.1016/j.coastaleng.2008.06.003>

548 Zakeri, A., Høeg, K., Nadim, F., 2009. Submarine debris flow impact on pipelines—Part II:
549 Numerical analysis. *Coastal Eng.*, 56 (1), 1–10.
550 <https://doi.org/10.1016/j.coastaleng.2008.06.005>

551 Zeinoddini, M., Bakhtiari, A., Ehteshami, M., Seif, M.S., 2016. Towards an understanding of the
552 marine fouling effects on VIV of circular cylinders: response of cylinders with regular
553 pyramidal roughness. *Appl. Ocean. Res.*, 59, 378–394.
554 <https://doi.org/10.1016/j.apor.2016.05.013>

555 Zhang, X., Oñate, E., Torres, S.A.G., Bleyer, J., Krabbenhoft, K., 2019a. A unified Lagrangian
556 formulation for solid and fluid dynamics and its possibility for modelling submarine
557 landslides and their consequences. *Comput. Method Appl. M.*, 343, 314–338.
558 <https://doi.org/10.1016/j.cma.2018.07.043>

559 Zhang, Y., Wang, Z., Yang, Q., Wang, H., 2019b. Numerical analysis of the impact forces exerted
560 by submarine landslides on pipelines. *Appl. Ocean. Res.*, 92, 101936.

- 561 <https://doi.org/10.1016/j.apor.2019.101936>
- 562 Zhao, E.J., Dong, Y.K., Tang, Y.Z., Sun, J.K., 2021. Numerical Investigation of Hydrodynamics
563 and Local Scour around Submarine Pipeline under Joint Effect of Solitary Wave and Current.
564 *Ocean Engineering*, 222, 108553. <https://doi.org/10.1016/j.oceaneng.2020.108553>
- 565 Zhou, B., Wang, X., Gho, W.M., Tan, S.K., 2015. Force and flow characteristics of a circular
566 cylinder with uniform surface roughness at subcritical Reynolds numbers. *Appl. Ocean. Res.*,
567 49, 20–26. <https://doi.org/10.1016/j.apor.2014.06.002>
- 568 Zhu, H., Randolph, M.F., 2011. Numerical analysis of a cylinder moving through rate-dependent
569 undrained soil. *Ocean Eng.*, 38 (7), 943–953. <https://doi.org/10.1016/j.oceaneng.2010.08.005>

570

Table captions

571 [Table 1](#). Herschel-Bulkley rheological model of submarine mudflows at 0.5 °C low-temperature

572 and mudflow impacting on pipeline conditions (modified after Guo et al. ([2020b](#))).

573 [Table 2](#). Specific settings of pipeline surface roughness.

574 [Table 3](#). Simulation results of the drag force coefficient under three Reynolds number conditions

575 in different studies.

576 [Table 1](#). Herschel-Bulkley rheological model of submarine mudflows at 0.5 °C low-temperature

577 and mudflow impacting on pipeline conditions (modified after Guo et al. (2020b))

Submarine mudflow physical and mechanical properties						Impact on pipeline characteristic parameters		
No.	Water content ω (ω/ω_L)	Density ρ (kg/m ³)	Herschel-Bulkley model			Velocity U_∞ (m/s)	Shear rate $\dot{\gamma} = \frac{U_\infty}{D}$ (s ⁻¹)	Reynolds number $Re_{\text{non-Newtonian}} = \frac{\rho \cdot U_\infty^2}{\tau}$
			τ_y (Pa)	K (Pa·s ^{<i>n</i>})	<i>n</i>			
1	90.0% (1.8)	1468	264.112	60.998	0.275	1.00	40	3.40
2	100.2% (2.0)	1423	137.068	28.646	0.320	0.25	10	0.45
3	123.8% (2.5)	1356	43.133	0.599	0.794	2.00	80	86.70
4	151.2% (3.0)	1312	11.867	0.118	1.000	2.50	100	346.47

578 where ω is the water content of the submarine mudflow; ω_L is the liquid limit of the submarine

579 mudflow; ρ is the density of the submarine mudflow (kg/m³); U_∞ is the velocity of the submarine

580 landslide (m/s); D is the diameter of the submarine pipeline; and $Re_{\text{non-Newtonian}}$ is the Reynolds

581 number of the submarine mudflow, which is dimensionless.

582

Table 2. Specific settings of pipeline surface roughness

Parameter	Symbol	Value			Unit	
Surface roughness	k_s	0	0.0015	0.015	0.15	mm
Pipeline diameter	D	25			mm	
Roughness diameter ratio	RDR	0	0.00006	0.0006	0.006	-

583 Note: the simulated working condition of 0.15 mm surface roughness is equivalent 6 mm coarse

584 sand on the surface of a submarine pipeline with 1 m diameter in actual engineering. In addition, a

585 submarine pipeline with a roughness of 0 mm means that the pipeline surface is nearly smooth.

586 [Table 3](#). Simulation results of the drag force coefficient under three Reynolds number conditions

587

in different studies

Studies	Reynolds number ($Re_{\text{non-Newtonian}}$)		
	2.08	6.67	10.08
Zakeri (2009)	13.07	4.15	2.96
Liu et al. (2015)	12.18	3.73	2.69
This paper	12.25	3.95	2.86

Figure captions

588

589 [Fig. 1](#). Geometry, grid and boundary conditions for the CFD modelling.

590 [Fig. 2](#). Equivalent sand grain roughness model; (a) applied to seabed; (b) applied to submarine
591 pipeline.

592 [Fig. 3](#). Impact forces as a function of time for suspended pipelines with different surface
593 roughness at Reynolds number 346.47.

594 [Fig. 4](#). Impact forces as a function of time for laid-on-seabed pipelines with different surface
595 roughness at Reynolds number 346.47.

596 [Fig. 5](#). Peak impact forces as a function of Reynolds number for different surface roughnesses.

597 [Fig. 6](#). Contours of (a) pressure and (b) shear rate for suspended pipelines with smooth and rough
598 ($k_s = 0.15$ mm) surfaces at selected instants in time and at Reynolds number 346.47.

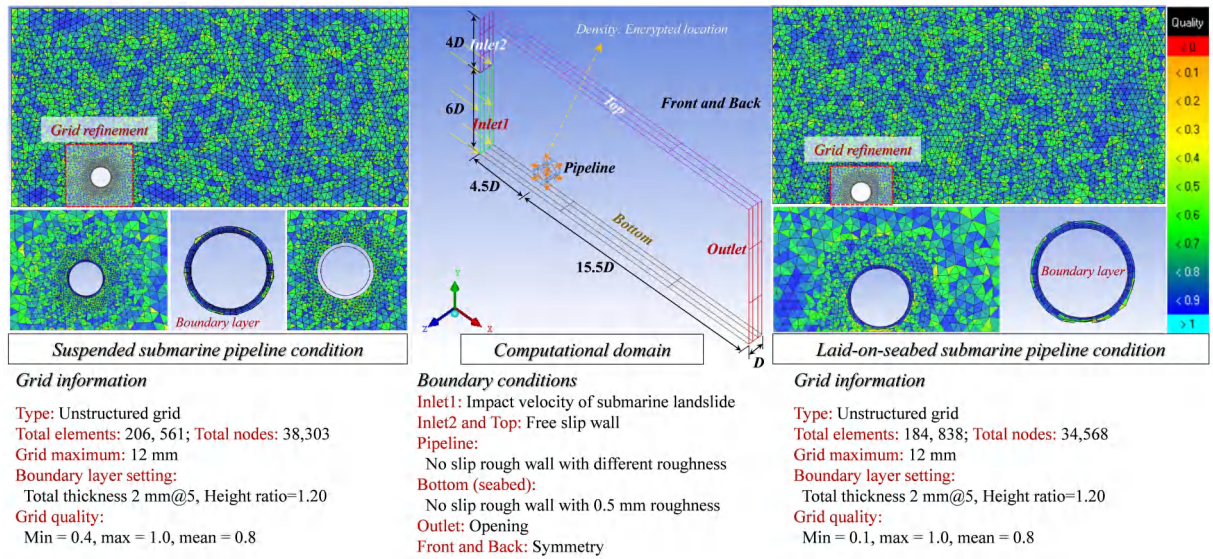
599 [Fig. 7](#). Contours of the (a) pressure and (b) shear rate for the laid-on-seabed pipelines with smooth
600 and rough ($k_s = 0.15$ mm) at selected instants in time and at Reynolds number 346.47.

601 [Fig. 8](#). Contours of velocity distribution for the suspended pipeline at Reynolds number 346.47; (a)
602 smooth pipeline; (b) pipeline with $k_s = 0.15$ mm.

603 [Fig. 9](#). Strouhal number as a function of Reynolds number.

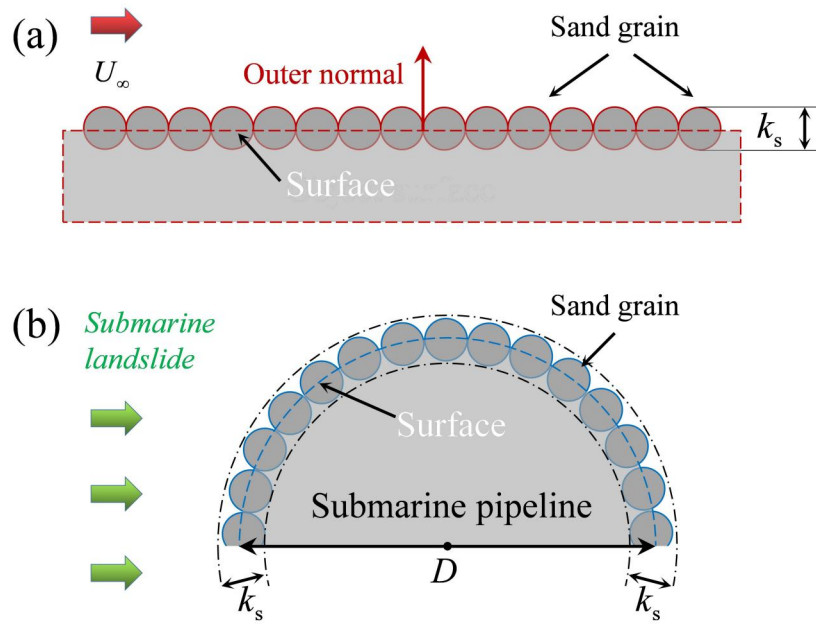
604 [Fig. 10](#). Peak impact force coefficients as a function of Reynolds number for different surface
605 roughnesses.

606 [Fig. 11](#). Standard evaluation charts for the surface roughness adjustment factor.



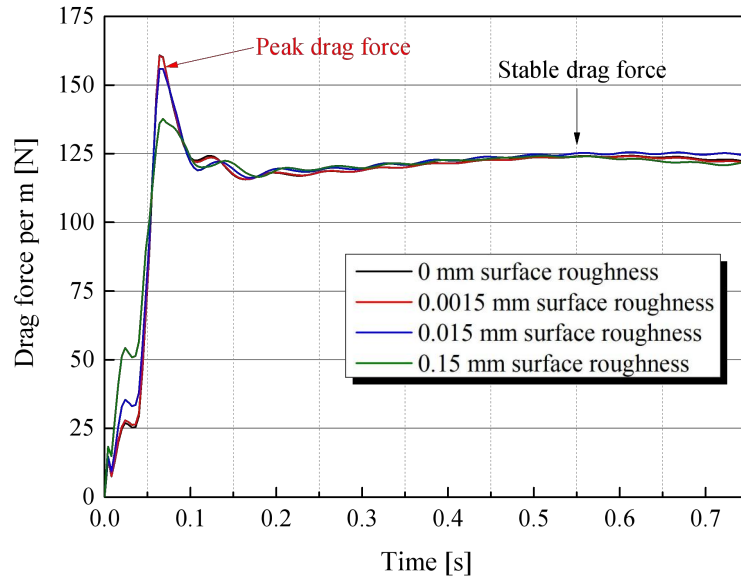
607

Fig. 1. Geometry, grid and boundary conditions for the CFD modelling



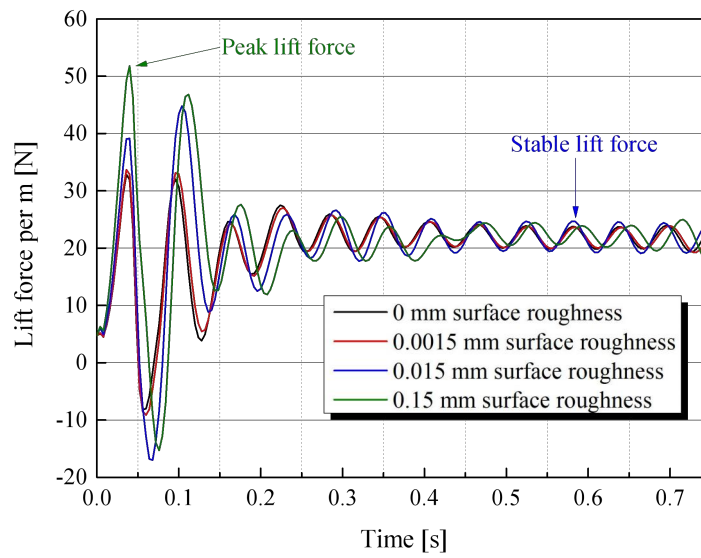
608 Fig. 2. Equivalent sand grain roughness model; (a) applied to seabed; (b) applied to submarine

609 pipeline



610

(a) Drag force



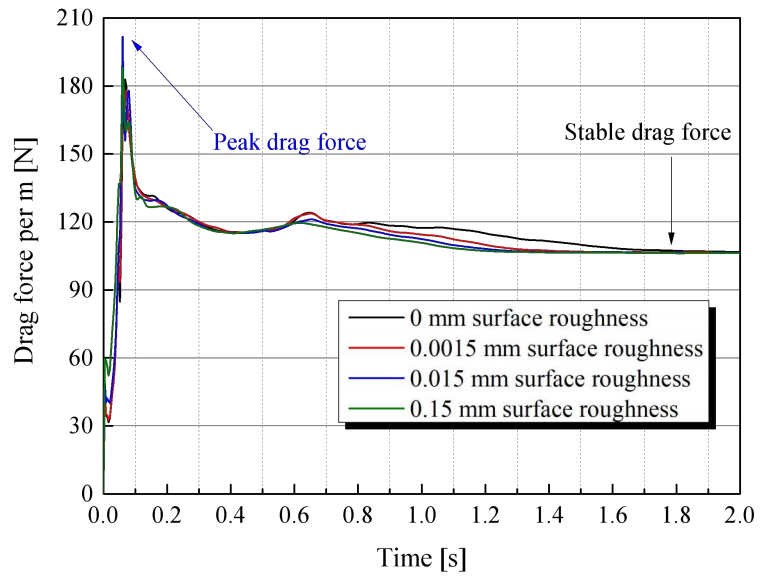
611

(b) Lift force

612 **Fig. 3.** Impact forces as a function of time for suspended pipelines with different surface

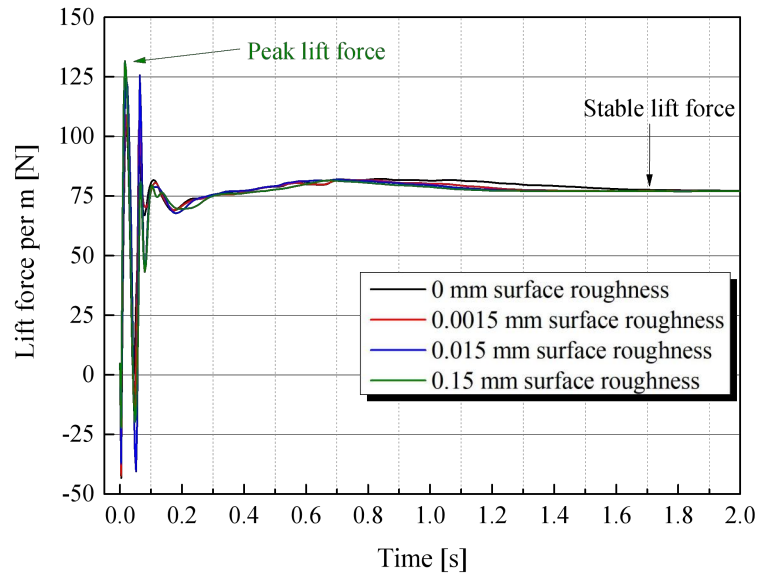
613

roughness at Reynolds number 346.47



614

(a) Drag force



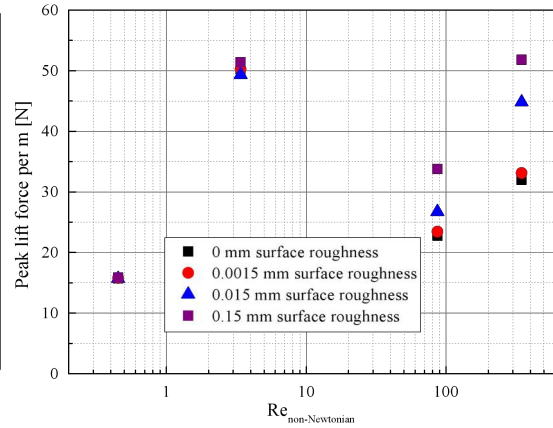
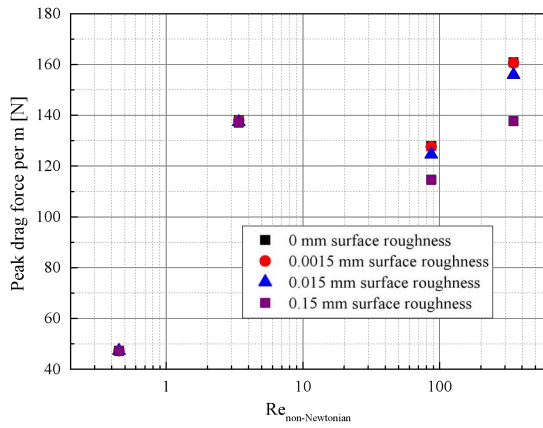
615

(b) Lift force

616 Fig. 4. Impact forces as a function of time for laid-on-seabed pipelines with different surface

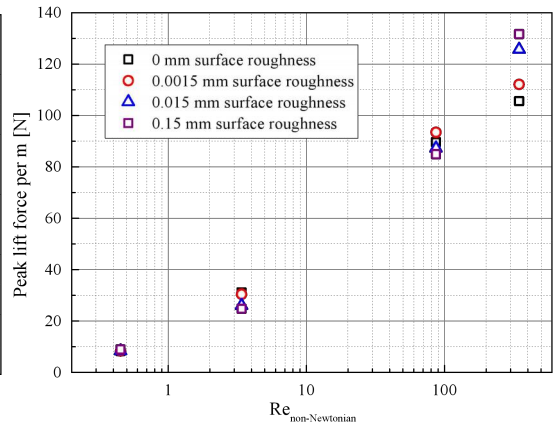
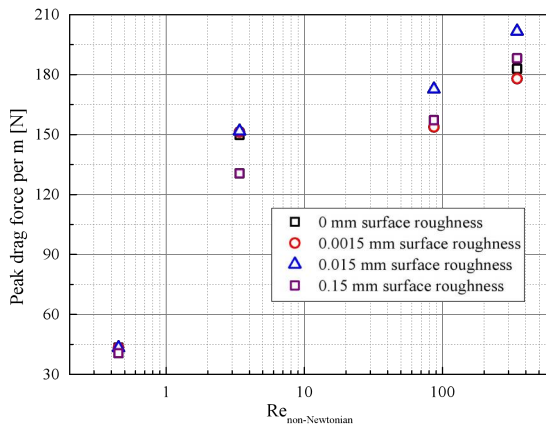
617

roughness at Reynolds number 346.47



618 (a) Peak drag force on suspended pipeline

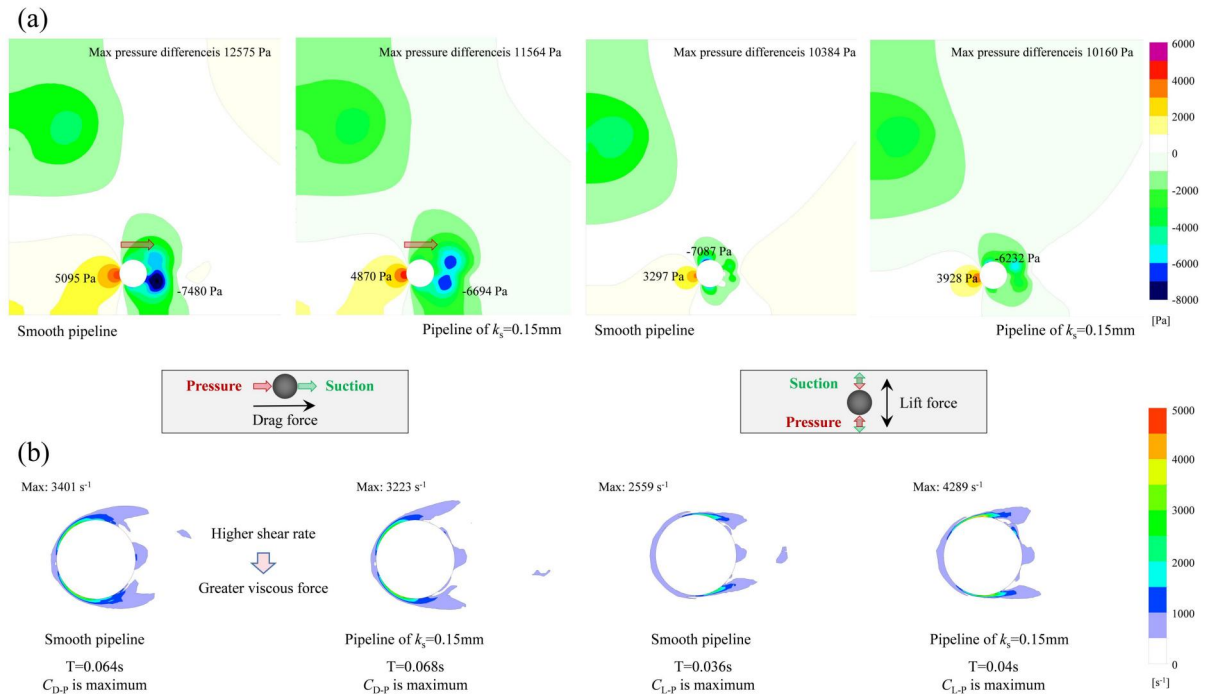
(b) Peak lift force on suspended pipeline



619 (c) Peak drag force on laid-on-seabed pipeline

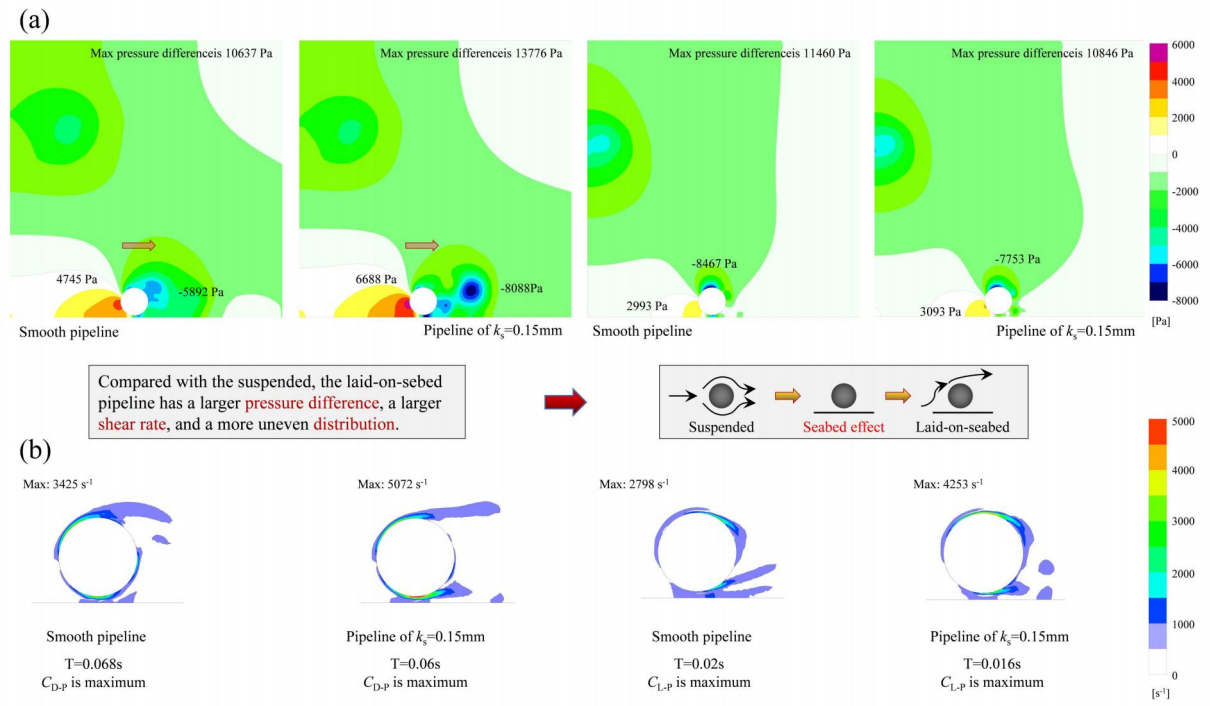
(d) Peak lift force on laid-on-seabed pipeline

620 Fig. 5. Peak impact forces as a function of Reynolds number for different surface roughnesses



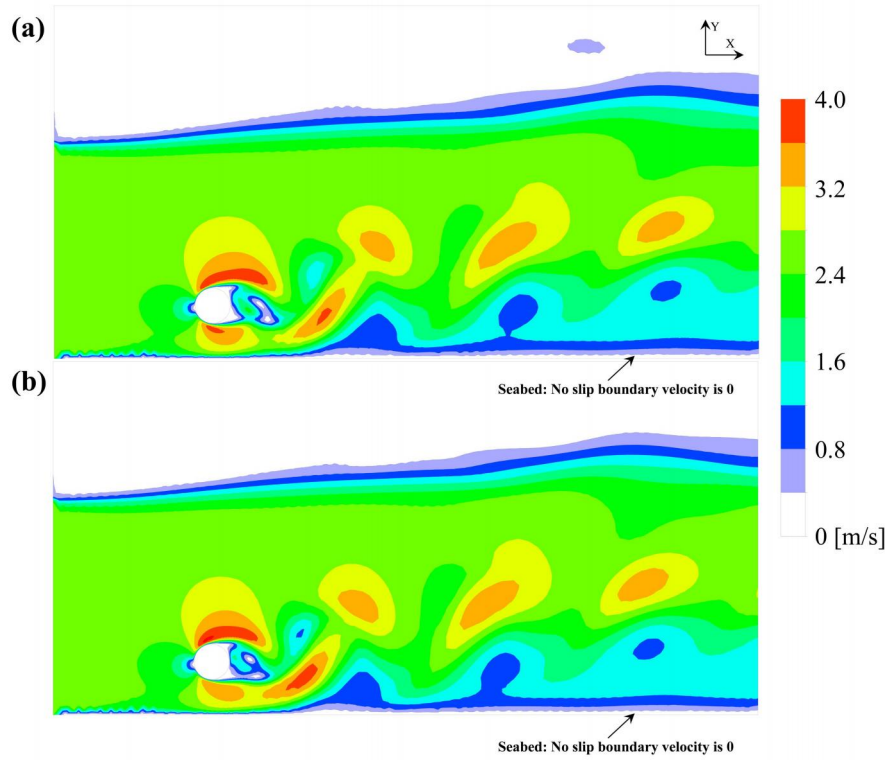
621 Fig. 6. Contours of (a) pressure and (b) shear rate for suspended pipelines with smooth and rough

622 ($k_s = 0.15\text{ mm}$) surfaces at selected instants in time and at Reynolds number 346.47



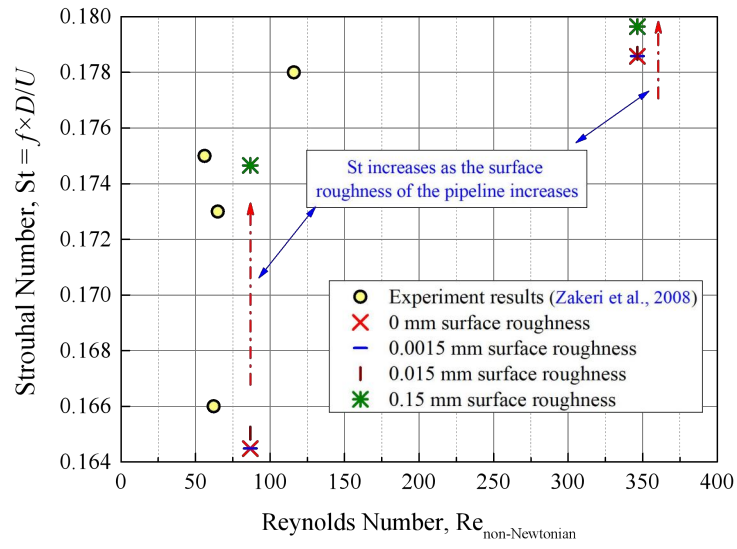
623 Fig. 7. Contours of the (a) pressure and (b) shear rate for the laid-on-seabed pipelines with smooth

624 and rough ($k_s = 0.15$ mm) at selected instants in time and at Reynolds number 346.47



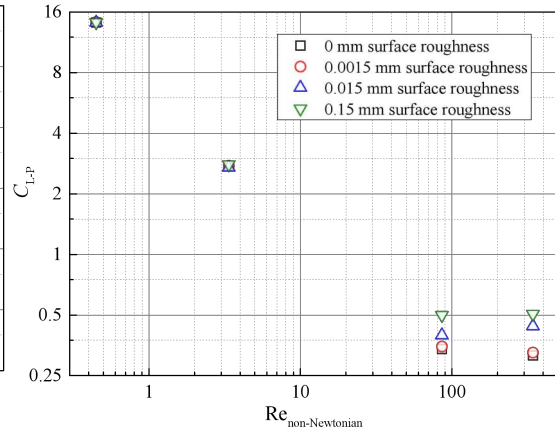
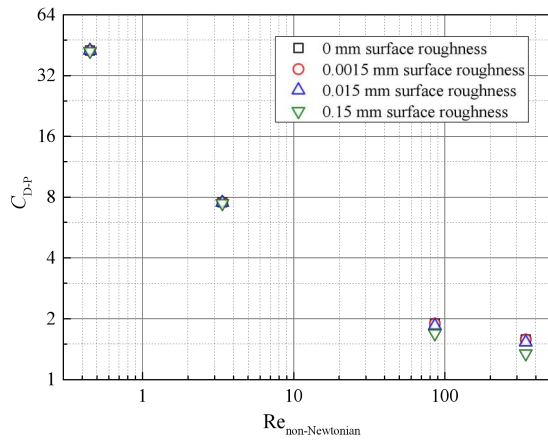
625 Fig. 8. Contours of velocity distribution for the suspended pipeline at Reynolds number 346.47; (a)

626 smooth pipeline; (b) pipeline with $k_s = 0.15$ mm



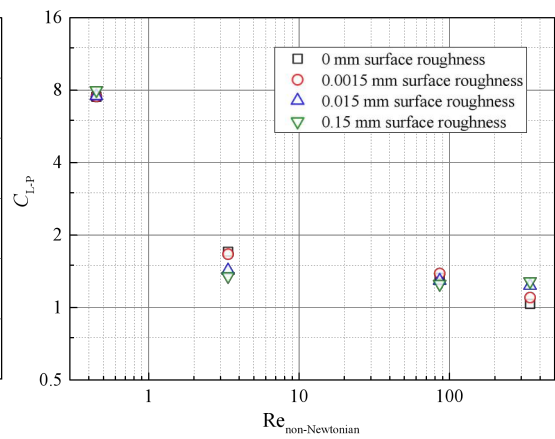
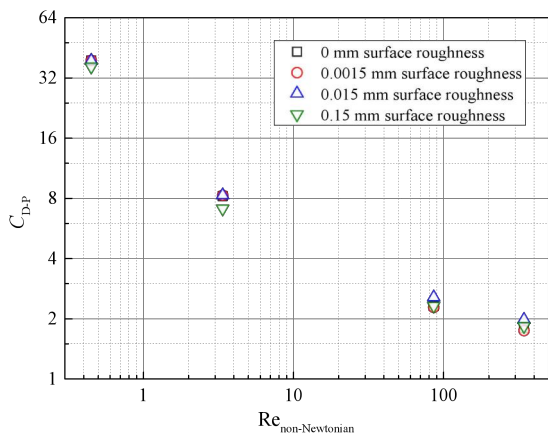
627

Fig. 9. Strouhal number as a function of Reynolds number



628 (a) C_{D-P} of suspended pipeline

(b) C_{L-P} of suspended pipeline

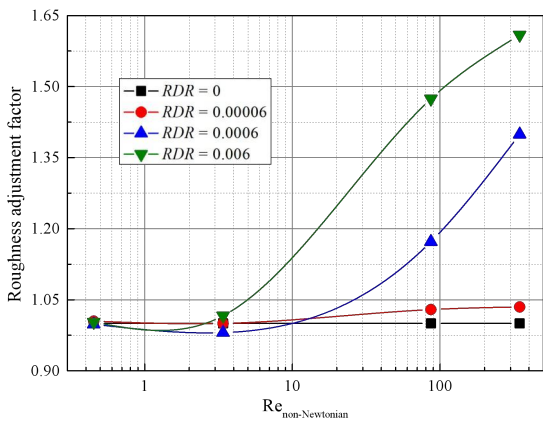
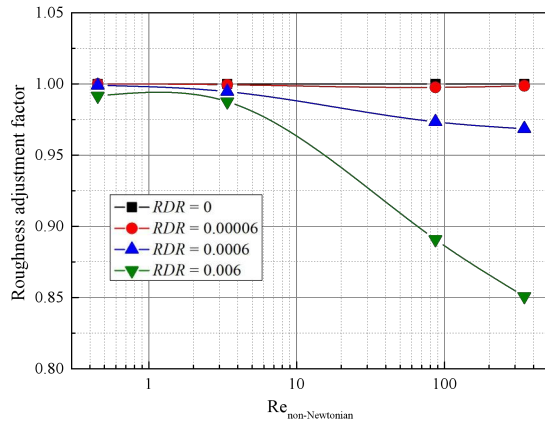


629 (c) C_{D-P} of laid-on-seabed pipeline

(d) C_{L-P} of laid-on-seabed pipeline

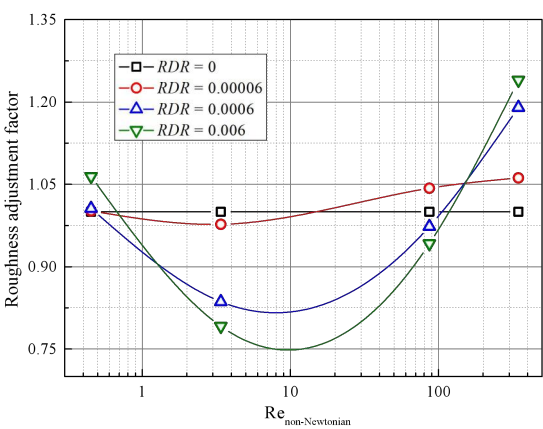
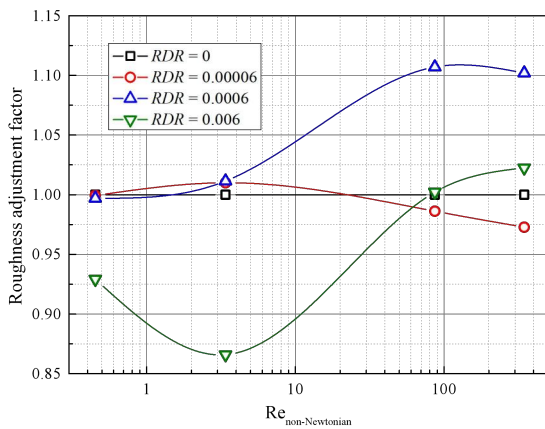
630 Fig. 10. Peak impact force coefficients as a function of Reynolds number for different surface

631 roughnesses



632 (a) Peak drag force on suspended pipeline

(b) Peak lift force on suspended pipeline



633 (c) Peak drag force on laid-on-seabed pipeline

(d) Peak lift force on laid-on-seabed pipeline

634 Fig. 11. Standard evaluation charts for the surface roughness adjustment factor